Science and Technology for Energy Transition **77**, 16 (2022)

https://doi.org/10.2516/stet/2022013

Selected Papers from 7th International Symposium on Hydrogen Energy, Renewable Energy and Materials (HEREM), 2021
Edited by Mohan Lal Kolhe

Available online at:
stet-review.org

REGULAR ARTICLE OPEN ACCESS

Inverse estimation of wall temperature measurement under dispersion medium shielding based on CMA-ES algorithm

Lin-Feng Qian[1,*], Yu-Kun Ji[2], Ze-Yu Zhu[2], Di Wu[1,*], Guang-Ming Xu[1] and Yong Huang[3]

[1] China Special Equipment Inspection and Research Institute, Beijing 100013, PR China
[2] School of Energy Science and Engineering, Harbin Institute of Technology, Harbin 150001, PR China
[3] School of Aeronautical Science and Engineering, Beihang University, Beijing 100191, PR China

Received: 5 November 2021 / Accepted: 21 April 2022

Abstract. Special equipment is often accompanied by the phenomenon of high temperature and high pressure in operation, and it needs to be measured. With the deepening of research engineering application, some new problems appear, such as how to accurately measure and control the combustion temperature field in the hydrocarbon energy system, carry out combustion diagnosis, control the combustion temperature, minimize the generation of pollutants, put forward higher requirements for measurement technology. High temperature has a core impact on equipment safety, which is a key index that must be considered in design and material selection. Near the surface of these high-temperature objects, there are usually high-temperature translucent media and particles produced by combustion, which have a great impact on radiation temperature measurement. At the same time, with the change of temperature and concentration, these translucent media often have gradient refractive index change, which has a certain impact on radiation temperature measurement. These shielding objects interfere with radiation and affect the accuracy of measurement. This topic mainly focuses on the theoretical and experimental research of this kind of problem. The inversion algorithm of wall temperature reconstruction under the shielding condition of dispersed medium is proposed. Under the condition of introducing different measurement errors, the algorithm is verified, and the corresponding numerical simulation is carried out to verify the feasibility of the algorithm model.

Keywords: Inverse radiation problem, Gradient refractive index, High-temperature measurement, Special equipment.

Nomenclature

κ_s	Scattering coefficient
χ	The derivative of the refractive index
$\mathbf{x}$	Individual
$\mathbf{m}$	The search distribution
g	Generation
μ	Number of individuals selected
c_1	Rank-one update coefficient
$\mathbf{y}$	The covariance matrix update
$\mathbf{P}_c$	The evolution path
μ_{eff}	The variance effective selection mass for the mean
E	Expected length
$\mathbf{I}$	The unity matrix
τ	Optical thickness
$\mathbf{S}$	Radiation source term
n	Refractive index
$F_{fitness}$	Objective function
I_{exp}	The directional radiation intensity calculated by simulation experiments
F_{obj}	The objective function
θ	Sampling angle
σ	The standard deviation
a_1, b_1, a_2, b_2	The coefficient of linear distribution
φ	The ratio of wall temperature to medium temperature
w	Positive weight coefficients
μ, μ'	Direction cosine
π	Pi
ω	Extinction coefficient
Ω	Solid angle
λ	Wavelength
$\sigma^{(g)}$	Step-size
$\mathbf{C}$	Covariance matrix

* Corresponding authors: qianlinfeng@csei.org.cn; wudi@csei.org.cn

f	The objective function
c_μ	The rank-μ update coefficient
h_σ	The Heaviside function
c_c	The learning rate
N	A multivariate normal distribution
d_σ	The damping parameter
ω_λ	Extinction coefficient
$\mathbf{\Phi}$	Scattering Phase Function
$\mathbf{\Omega}$	Direction vector
L	Plate thickness
I_{est}	The directional radiation intensity calculated according to the solution vector
i	Grid index of the cell
I_*	The outgoing radiation or radiation response signal
ς	The standard normally distributed random number
X	The value of the parameters to be inverted
x	The normalized spatial position
δ	A small rate of change
κ_a	Absorption coefficient, m^{-1}
σ	Stefan–Boltzmann constant $5.67 \times 10^{-8}\ \text{W}/(\text{m}^2 \cdot \text{K}^4)$

1 Introduction

A large amount of heat generated in the combustion process of power plant boilers is mainly transmitted to the medium in the form of radiation, convection, and heat conduction [1]. Combustion is a violent chemical reaction process and the primary process of energy conversion. For furnace flame, high-temperature flue gas and metal temperature of boiler or heat exchanger are some of the important factors to measure the stability of combustion and operation condition. On fire or high-temperature objects in radiation temperature measurement technology involves internal radiation transmission and many problems [2]. The calculation of radiative transfer in participatory media usually assumes that the refractive index of a flame uniform field, namely the spread of the light always along a straight-line trajectory through the research object. So although to some extent simplifies the calculation process and improves the computational efficiency. However, the refractive index tends to be unevenly distributed due to the uneven spatial distribution of the temperature, pressure, or composition of the flame [3]. If the refraction index distribution of semi-transparent high-temperature mediums such as flame and high-temperature flue gas is regarded as uniform for temperature field reconstruction, the measurement accuracy and measurement range will inevitably be reduced. For metal temperature receiving radiant heat or being scoured by high-temperature flue gas, high precision temperature measurement is also required in operation. Due to the presence of flame or high-temperature smoke and other participating media on its surface, the influence of gradient refractive index formed by the change of temperature and concentration on the temperature measurement results cannot be ignored [4–6]. Therefore, it is of great scientific and practical value to study the refractive index gradient distribution and its influence on radiation transfer in flame or high-temperature semi-transparent medium in actual production.

Among many temperature measurement technologies, based on features of flame radiation on temperature field inversion temperature measurement technology is the new development direction with a relatively simple device, the measurement is relatively direct, the advantage of high reliability. Such as light-field imaging technology, its core is still the image method used to obtain the boundary of the flame radiation intensity distribution, the temperature, and optical parameters inversion. At present, light field imaging technology has great development space in the field of combustion diagnosis [7]. Essentially, it can be concluded as the reconstruction of multiple physical quantity fields in a high-temperature medium based on space radiation light field information. This is a typical radiation inverse problem with obvious discomfort [8], so it is quite difficult to solve it.

There is usually a translucent medium between the measured object and the probe in the research of furnace flame or high-temperature object temperature measurement technology. Precise gradient refractive index medium of these areas is involved in the information transmission process of field which can give people more in-depth understanding of the radiation energy transfer mechanism and the radiation law of information transmission and master the gradient refractive index medium radiation transmission characteristics of field related optimization design method, manufacture technology and measurements [8–12]. Therefore, there is important theoretical significance engineering application value in studying the radiation characteristics and temperature measurement technology under the condition of gradient refractive index medium shielding.

Radiative transfer in graded refractive index media is much more complex than that in uniform refractive index media. Light in a uniform refractive index medium travels along a straight line. But in a gradient refractive index medium, the light will travel along a curved path, and sometimes even total reflection will occur inside the medium [13]. Therefore, the traditional radiative transfer method for uniform refractive index media cannot be directly applied to solve the radiative transfer in graded refractive index media. In recent years, the radiative transfer in graded refractive index media has attracted more and more attention from scholars all over the world.

Methods for calculating radiation transfer in graded refractive index media include Discrete Ordinates Method (DOM) [14–16], Finite Volume Method (FVM) [3, 17, 18], Finite Element Method (FEM) [19, 20], Spectral Element Method (SEM) [21, 22], etc. The global discretization method based on differential form radiative transfer equation can be used to deal with multi-dimensional complex geometric area problems conveniently and economically and complex medium and boundary characteristics problems flexibly. It can also be easily used to solve the coupled heat transfer problems of radiation, heat conduction, and convection. Especially for the finite volume method and discrete coordinate method because of their strong adaptability.

Wei *et al.* studied the inverse estimation of refractive index related to temperature/phase transition in translucent media. The refractive index is inverted from the radiative response of the boundary by a Stochastic Particle Swarm Optimization (SPSO) algorithm. Through the sensitivity analysis, it is proved that this method can accurately deduce the refractive index from the radiation response on the two boundaries [23]. Zhao *et al.* studied linear and nonlinear gradient refractive index distributions based on discrete coordinate equations. Temperature and radiative heat flow distribution in isotropic and heterotropic media [24], transient radiative transfer equation [25, 26], and coupled radiative heat transfer in multi-dimensional homogeneous media with arbitrarily complex shapes were solved by spectral element method. Wei *et al.* found that the refractive index and absorption coefficient differ in sensitivity to boundary conditions, making it difficult to estimate spatially correlated refractive index and absorption coefficient simultaneously. A two-step inversion model with different laser irradiations is proposed for this problem [27].

Although the combustion heat transfer problem has been solved by combining theory with experience. It has been widely used in large power station boilers and industrial combustion devices. With the deepening of research engineering application, some new problems appear, such as how to accurately measure and control the combustion temperature field in the hydrocarbon energy system, carry out combustion diagnosis, control the combustion temperature, minimize the generation of pollutants, put forward higher requirements for measurement technology.

This paper mainly focuses on the influence of passive radiation on the temperature measurement of flame and boiler components under the condition of translucent medium with a gradient refractive index. The reconstruction program of gradient absorption coefficient and refractive index of functional distribution is established based on Evolution Strategy based on Covariance Matrix Adaption (CMA-ES) algorithm. The temperature ratio was defined and the sensitivity of distribution function coefficients was analyzed under different temperature ratios, outgoing radiation, and different surface normal angles to obtain a better combination of measurement information. The temperature ratio and the included angle are selected according to the graph line of sensitivity coefficient. The form of the distribution function of the gradient absorption coefficient and refractive index of the discrete distribution in the process of reconstruction is unknown to consider the more general distribution of photothermal parameters. The sensitivity of absorption coefficient and refractive index is analyzed for the two-layer medium model. The sensitivity graph of absorption coefficient and refractive index of the three-layer medium model is analyzed and explained the rationality of the image drawn. An inversion algorithm for wall temperature reconstruction with variable refractive index medium is proposed.

2 Direct problem

Consider an absorbing, emitting, and scattering 1D parallel-plane medium with variable refractive index and azimuthally symmetric radiation bounded by two diffusely reflecting plates. As shown in Figure 1, both sides of the boundary are assumed to be the diffuse gray opaque wall with the same emissivity. The left and the right boundary walls are subjected to the first kind of boundary condition with constant temperature T_0 and T_L respectively. The absorption coefficient and scattering coefficient are supposed to be constant. The refractive index $n(x)$ varies with axis x.

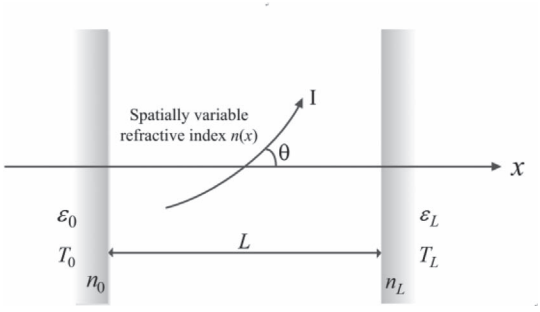

Fig. 1. The physical model of radiative heat transfer in 1D participating media with GRI.

The radiative transfer equation in a 1D participating media with graded-index in Cartesian coordinate can be expressed as,

$$\mu\frac{\partial I(x,\mu)}{\partial x}+\chi\left(1-\mu^2\right)\frac{\partial I(x,\mu)}{\partial \mu}+(\kappa_a+\kappa_s-2\chi\mu)I(x,\mu)=$$

$$n^2\kappa_a I_b+\frac{\kappa_s}{2}\int_{-1}^{1}I(x,\mu')\,\Phi(\mu',\mu)\mathrm{d}\mu'. \quad (1)$$

Boundary conditions for grey-diffuse walls can be expressed as,

$$I(0,\mu)=\varepsilon_0 n_0^2\frac{\sigma T_0^4}{\pi}+2(1-\varepsilon_0)\int_{-1}^{0}I(0,\mu')\mu'\,\mathrm{d}\mu',\quad \mu\geq 0, \quad (2)$$

$$I(L,\mu)=\varepsilon_L n_L^2\frac{\sigma T_L^4}{\pi}+2(1-\varepsilon_L)\int_{0}^{1}I(L,\mu')|\mu'|\mathrm{d}\mu',\quad \mu<0, \quad (3)$$

where $I(x,\ \mu)$ is radiation intensity at position x and direction cosine μ, I_b is the blackbody radiation intensity at the temperature of the media $T(x)$, $\Phi(\mu',\ \mu)$ is the scattering phase function of energy transfer from an incoming direction cosine μ' to an outgoing direction cosine μ, σ is Stefan–Boltzmann constant, κ_a is the absorption coefficient, κ_s is the scattering coefficient and χ means the derivative of the refractive index after natural logarithm to the coordinate x,

$$\chi=\frac{\mathrm{d}(\ln\ n)}{\mathrm{d}x}. \quad (4)$$

3 Inverse problem

3.1 CMA-ES algorithm

The CMA-ES algorithm has been developed to be a well-established algorithm system that contains many variants

for different types of problems with the efforts of Hansen, Ostermeier, and their colleagues [28–30]. In this study, the integral equations of light scattering signals need to be deconvoluted to reconstruct the size distribution and morphological parameters. Mathematically, it is a typical ill-conditioned multiple dimensional non-separable inverse problem. Given the good performance of CMA-ES in solving the ill-conditional and non-separable problems [29–31], this promising algorithm is suitable to solve the inverse problem of light scattering. What follows is a brief introduction of the theoretical fundamentals of the CMA-ES algorithm, heavily based on a tutorial written by Hansen [29] which the reader can refer to for a full and detailed derivation.

In the CMA-ES, if the number of objective parameters to be inverted is n, then the search point is an n-dimensional vector, which is also called the objective vector. The basic equation of CMA-ES is to generate the new search points by sampling a multivariate distribution [29]:

$$\mathbf{x}_k^{(g+1)} \sim \mathbf{m}^{(g)} + \sigma^{(g)} N\left(\mathbf{0}, \mathbf{C}^{(g)}\right) \quad \text{for } k = 1, \ldots, \lambda, \tag{5}$$

where $\mathbf{x}_k^{(g+1)} \in R^n$ is the kth offspring individual in the population of λ new search points at generation $g+1$, ~ denotes the same distribution on the left and right side, $\mathbf{m}^{(g)} \in R^n$ is the mean value of the search distribution at generation g, $\sigma^{(g)} \in R^n$ is the step-size at generation g, $N\left(\mathbf{0}, \mathbf{C}^{(g)}\right)$ denotes a multivariate normal distribution with zero mean and covariance matrix $\mathbf{C}^{(g)}$, *and* $\boldsymbol{m}^{(g)} + \sigma^{(g)} N(\mathbf{0}, \mathbf{C}^{(g)})$, $\boldsymbol{C}^{(g)} \in R^{n \times n}$ is the covariance matrix at generation g, $\lambda \geq 2$ is the population size or the number of the offspring individuals. The kernel of CMA-ES is to update distribution parameters $\mathbf{m}^{(g)}$, $\sigma^{(g)}$ and $\mathbf{C}^{(g)}$. *Update of the mean value* $\boldsymbol{m}^{(g)}$ is achieved by selection and recombination, which means the new mean $\mathbf{m}^{(g+1)}$ of the search distribution is a weighted average of μ selected points from samples $\mathbf{x}_1^{(g+1)}$, $\mathbf{x}_2^{(g+1)}$,…, $\mathbf{x}_\lambda^{(g+1)}$ [29]:

$$\mathbf{m}^{(g+1)} = \sum_{i=1}^{\mu} w_i \mathbf{x}_{i:\lambda}^{(g+1)}, \tag{6}$$

where $\mu \leq \lambda$ is the parent population size, *i.e.* the number of selected points, $w_{i=1\ldots\mu} \in \mathbb{R}^+$ are positive weight coefficients for recombination such that $w_1 \geq w_2 \geq \ldots \geq w_\mu > 0$ and $\Sigma w_i = 1$; $\mathbf{x}_{i,\lambda}^{(g+1)}$ is the ith best individual out of $\mathbf{x}_1^{(g+1)}$, $\mathbf{x}_2^{(g+1)}$,…, $\mathbf{x}_\lambda^{(g+1)}$ and the index i. λ denotes the index of the ith ranked individual, the "best" and "ranked" individuals are both defined by their objective function value. The smaller the individual's objective function value is, the better the individual is, and the higher its ranking is $f\left(\mathbf{x}_{1:\lambda}^{(g+1)}\right) \leq f\left(\mathbf{x}_{2:\lambda}^{(g+1)}\right) \leq \cdots \leq f\left(\mathbf{x}_{\lambda:\lambda}^{(g+1)}\right)$ where f is the objective function to be minimized.

The update of the covariance matrix is realized by the covariance matrix adaption based on rank-μ update and rank-one update. The rank-μ update aims to give the estimation of covariance matrix reliable for the small

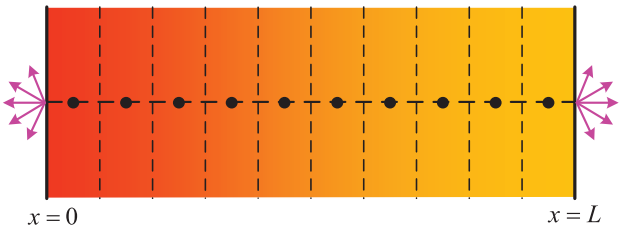

Fig. 2. One-dimensional translucent plate model.

population. The rank-one update means that there is only one search point per generation for updating the covariance matrix in limited cases. Finally, rank-μ update and rank-one update are combined to generate a new covariance matrix [29]:

$$\mathbf{C}^{(g+1)} = \underbrace{\left(1 + c_1\delta(h_\sigma) - c_1 - c_\mu \sum_{i=1}^{\lambda} w_i\right)}_{\text{can be close or equal to 0}} \mathbf{C}^{(g)}$$

$$+ c_1 \underbrace{\mathbf{p}_c^{(g+1)} \left[\mathbf{p}_c^{(g+1)}\right]^T}_{\text{rank-one update}} + c_\mu \underbrace{\sum_{i=1}^{\lambda} w_i \mathbf{y}_{i:\lambda}^{(g+1)} \left[\mathbf{y}_{i:\lambda}^{(g+1)}\right]^T}_{\substack{\text{rank} \\ \text{update}}}, \tag{7}$$

where $c_\mu \leq 1 - c_1$ is the learning rate for the rank-μ update of the covariance matrix update, $c_1 \leq 1 - c_\mu$ is the learning rate for the rank-one update of the covariance matrix update, $\mathbf{y}_{i:\lambda}^{(g+1)} = \left(\mathbf{x}_{i:\lambda}^{(g+1)} - \mathbf{m}^{(g)}\right)/\sigma^{(g)}$, h_σ is the Heaviside function, $\delta(h_\sigma) = (1 - h_\sigma)c_c\ (2 - c_c) \leq 1$, $\mathbf{p}_c^{(g+1)} \in \mathbb{R}^n$ is the evolution path at generation $g+1$. The evolution path can be expressed by a sum of consecutive steps which is referred to as cumulation [29]:

$$\mathbf{p}_c^{(g+1)} = (1 - c_c)\mathbf{p}_c^{(g)} + h_\sigma \sqrt{c_c(2 - c_c)\mu_{\text{eff}}} \frac{\mathbf{m}^{(g+1)} - \mathbf{m}^{(g)}}{\sigma^{(g)}}, \tag{8}$$

where $c_c \leq 1$ is the learning rate for cumulation for the rank-one update of the covariance matrix, μ_{eff} denotes the variance effective selection mass for the mean. The factor $\sqrt{c_c(2 - c_c)\mu_{\text{eff}}}$ is a normalization constant for $\mathbf{p}_c$.

The evolution path is also utilized to control the step size. Unlike equation (8), applying the same technique in equation (9) is to build a conjugate evolution path as [29]:

$$\mathbf{p}_\sigma^{(g+1)} = (1 - c_\sigma)\mathbf{p}_\sigma^{(g)} + \sqrt{c_\sigma(2 - c_\sigma)\mu_{\text{eff}}} \left(\boldsymbol{C}^{(g)}\right)^{-0.5} \frac{\mathbf{m}^{(g+1)} - \mathbf{m}^{(g)}}{\sigma^{(g)}}, \tag{9}$$

where $\mathbf{p}_\sigma^{(g)} \in \mathbb{R}^n$ is the conjugate evolution path at generation g, $c_\sigma < 1$ is the learning rate for the cumulation for the step-size control, $\sqrt{c_\sigma(2 - c_\sigma)\mu_{\text{eff}}}$ is a normalization constant, $\left(\mathbf{C}^{(g)}\right)^{-0.5} = \mathbf{B}^{(g)}\left(\mathbf{D}^{(g)}\right)^{-1}\left(\mathbf{B}^{(g)}\right)^{\mathrm{T}}$, where $\mathbf{C}^{(g)} = \mathbf{B}^{(g)}\left(\mathbf{D}^{(g)}\right)^2\left(\boldsymbol{B}^{(g)}\right)^T$ is an eigen decomposition of $\mathbf{C}^{(g)}$.

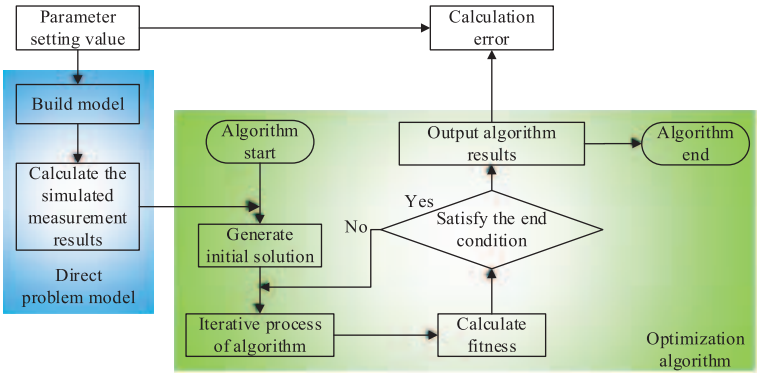

Fig. 3. Flow chart of inversion experiment.

Table 1. Average calculation results and errors of running tests.

		$a_1 = 4$	$a_2 = -19$	$a_3 = 15$
$\gamma = 0$	Calculation result	$4.00 \pm 8.98 \times 10^{-16}$	$-19.00 \pm 1.39 \times 10^{-14}$	$15.00 \pm 5.48 \times 10^{-15}$
	Error (%)	1.59×10^{-7}	2.87×10^{-8}	1.27×10^{-7}
$\gamma = 1\%$	Calculation result	$4.00 \pm 2.80 \times 10^{-4}$	$-19.01 \pm 5.02 \times 10^{-3}$	$15.00 \pm 1.81 \times 10^{-3}$
	Error (%)	0.10	0.04	0.01
$\gamma = 3\%$	Calculation result	$3.99 \pm 1.62 \times 10^{-3}$	$-18.93 \pm 3.53 \times 10^{-2}$	$14.95 \pm 1.47 \times 10^{-2}$
	Error (%)	0.36	0.38	0.34
$\gamma = 5\%$	Calculation result	$3.99 \pm 1.51 \times 10^{-3}$	$-18.89 \pm 4.52 \times 10^{-2}$	$14.91 \pm 2.18 \times 10^{-2}$
	Error (%)	0.36	0.59	0.62
$\gamma = 7\%$	Calculation result	$3.97 \pm 1.20 \times 10^{-2}$	$-18.84 \pm 2.28 \times 10^{-1}$	$14.90 \pm 9.47 \times 10^{-2}$
	Error (%)	0.77	0.82	0.64

To update the step-size $\sigma^{(g)}$, the matrix norm of conjugate evolution path $||\mathbf{p}_\sigma^{(g+1)}||$ is compared with its expected length $E\,||N(\mathbf{0}, \mathbf{I})||$, that is [29]:

$$\sigma^{(t+1)} = \sigma^{(t)} \exp\left[\frac{c_\sigma}{d_\sigma}\left(\frac{||\mathbf{p}_\sigma^{(t+1)}||}{E\,||N(\mathbf{0},\mathbf{I})||} - 1\right)\right], \tag{10}$$

where $d_\sigma \approx 1$ is the damping parameter for the step-size update, $\mathbf{I}$ is the unity matrix. In the present study, the strategy parameters settings of CMA-ES are available in [29].

To verify the performance of the CMA-ES algorithm in the inversion of medium photothermal parameters based on the inverse radiation problem, the forward radiation problem model of a one-dimensional translucent plate considering self-radiation is selected to construct the radiation inverse problem. The CMA-ES algorithm is tested from three aspects: the calculation time, the calculation results, and the value of the body-fitting function. The direct problem model and the inversion experiment flow are introduced below. The schematic diagram of the model is shown in Figure 2.

Only the absorption and emission characteristics of the medium are considered, L is the thickness of the medium, which is set as 1 m. κ is the absorption coefficient, which is set as 1.5 m^{-1}. Both sides of the medium are free boundaries. The radiative transfer equation is shown in equation (11):

$$\frac{dI_\lambda(\tau_\lambda)}{d\tau_\lambda} = -I_\lambda(\tau_\lambda) + (1-\omega_\lambda)I_{b\lambda}(\tau_\lambda) + \frac{\omega_\lambda}{4\pi} \times \int_{4\pi} I_\lambda\left(\tau_\lambda, \vec{\Omega}'\right)\Phi_\lambda\left(\vec{\Omega}', \vec{\Omega}\right)d\Omega', \tag{11}$$

where ω_λ is the extinction coefficient. The second and third terms on the right side of the equation contain the scattering caused by emission and incident in all directions of space, which is collectively known as the source function. The source function is,

$$S_\lambda(\tau_\lambda, \omega_\lambda) = (1-\omega_\lambda)I_{b\lambda}(\tau_\lambda) + \frac{\omega_\lambda}{4\pi} \times \int_{4\pi} I_\lambda\left(\tau_\lambda, \vec{\Omega}'\right)\Phi_\lambda\left(\vec{\Omega}', \vec{\Omega}\right)d\Omega'. \tag{12}$$

The radiation transfer equation in source function form can be written as,

$$\frac{dI_\lambda(\tau_\lambda)}{d\tau_\lambda} + I_\lambda(\tau_\lambda) = S_\lambda(\tau_\lambda, \omega_\lambda). \tag{13}$$

The flow chart of the inversion experiment is shown in Figure 3. The test was carried out at the same wavelength.

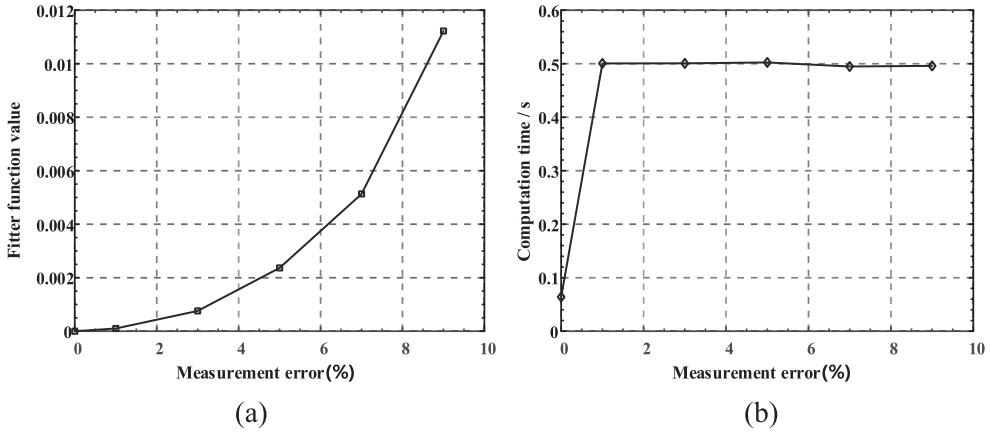

Fig. 4. Fitness function values and calculation time statistics of running tests. (a) Fitter function value, (b) computation time.

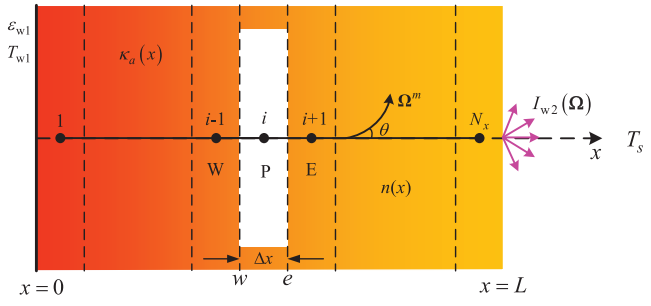

Fig. 5. A physical model of radiation heat transfer in one-dimensional inhomogeneous disseminated media considering radiation from one sidewall.

It was assumed that the radiation source function was independent of the extinction coefficient and was only a quadratic polynomial of the optical thickness. The testing process mainly includes a direct problem model and optimization algorithm. During the test, the input parameter values were assumed first to be used to substitute the direct problem model to calculate the simulated measurement results. A total of 10 measurement signals were taken as the measurement results, including 5 backward radiation signals on the left boundary and 5 forward radiation signals on the right boundary. Then, the simulation measurement results and the direct problem model are brought into the optimization algorithm, and the optimization result is obtained through iterative calculation. The objective function of the optimization algorithm is,

$$F_{\text{fitness}} = \sum_{i=1}^{10} \left(\frac{I_{\text{est}}}{I_{\text{exp}}} - 1 \right)^2, \tag{14}$$

where the subscript "est" and "exp" represent the directional radiation intensity calculated according to the solution vector and the directional radiation intensity calculated by simulation experiments, respectively. Finally, the error of the optimization result is calculated according to the assumed values of the input parameters.

This paper uses assumed parameters to test the CMA-ES algorithm, including no measurement error, adding 1%, 5%, 10%, 7% measurement error, and conditional 3% measurement error. During the process, the optimization algorithm was independently run 10 times, the average calculation time, success rate, average calculation result, and average calculation error were statistically analyzed. The search interval of the algorithm is [−20, 20].

Table 1 shows the average calculation results and errors of the source function coefficient inversion program of the radiation transfer equation based on the CMA-ES algorithm running independently 10 times. From the standard deviation of the calculated results, the results of the 10 independent measurements are relatively close which indicates that the algorithm has converged at the end of the operation. When no measurement error is added, the program can calculate more accurate measurement results. With the increase of addition error, the inversion error increases gradually and the increased amplitude is relatively slow. When 7% measurement error is added, that is the maximum measurement error adopted in this paper. The maximum error of inversion results is only 0.82%. It can be seen that the CMA-ES algorithm has high robustness in radiation inverse problems and the inversion results are less affected by measurement error.

The average fitter function value statistics and average computing time statistics of 10 independent runs of the inversion program are analyzed in Figure 4. As can be seen from the left figure, although the fitness function value obtained by the optimization algorithm increases exponentially with the increase of measurement error, the fitness function value corresponding to adding 9% measurement error is only 0.112. It can be seen from the picture on the right, after adding the error of measurement, calculation time is around 0.5 s, namely under different measurement errors, the number of iterations of the same algorithm running. This algorithm can be attributed to the unique parameter selection mechanism, namely the CMA-ES algorithm by the number of iterations and by the inversion parameters calculated, but this does not affect the convergence of the algorithm itself.

In summary, the CMA-ES algorithm has high robustness, strong optimization ability, and high computational efficiency when applied to the radiation inverse problem field. It is verified that the algorithm used in this paper is

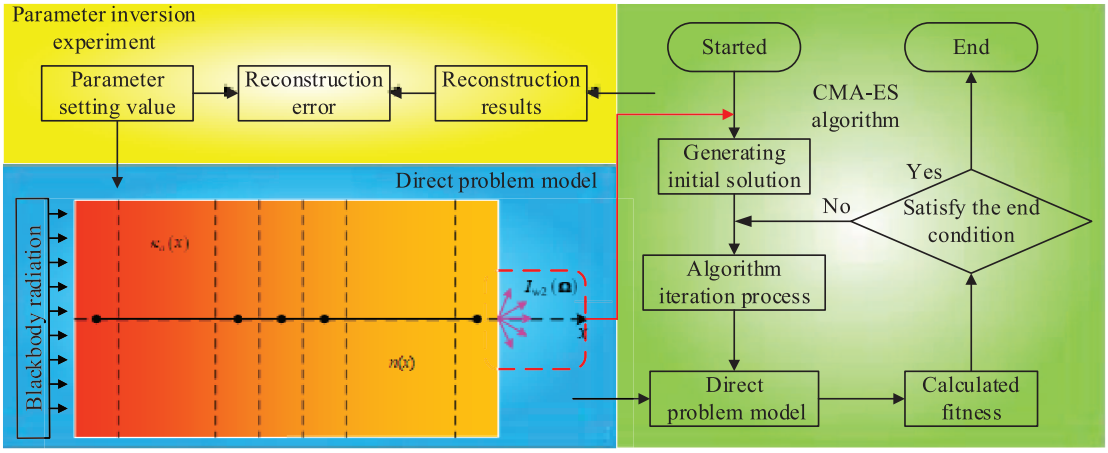

Fig. 6. Inversion model of photothermal parameters of dispersed media.

correct to invert the photothermal characteristic parameters of the inhomogeneous dispersion medium.

3.2 Inverse process

In general, the photothermal characteristic parameters of the dispersion medium are inhomogeneous. This section studies the inversion of the radiation characteristic parameters such as the absorption coefficient and refractive index of the dispersion medium. The one-dimensional radiative heat transfer model of inhomogeneous dispersion medium considering unilateral wall radiation is shown in Figure 5. The left side is the opaque boundary. In this study, it is assumed that the wall emissivity is taken, and the right side is the free boundary. The absorption coefficient and refractive index of the dispersion medium vary with the spatial position.

Based on the evolutionary strategy algorithm of the adaptive covariance matrix tested above, this paper constructed a reconstruction algorithm for the photothermal characteristic parameters (including absorption coefficient and refractive index) of the heterogeneous dispersion medium. The inversion model of the photothermal parameters of the dispersion medium is shown in Figure 6. In the figure, the three colors respectively represent three important components of the non-model, namely the direct problem model, CMA-ES algorithm, and parameter inversion experiment. The direct problem model part refers to the previous content. In the algorithm part, as the input of the algorithm, the radiation response signals in different directions on the right boundary at different wall temperatures are selected as the measurement information. Based on the CMA-ES algorithm, the gradient refractive index and absorption coefficient distribution of semi-transparent media were reconstructed. The selected objective function is as follows:

$$F_{\text{obj}} = \sum_{i=1}^{M} \sum_{j=1}^{N} \left\| \frac{I_{\text{est}}(T_i, \theta_j)}{I_{\text{exp}}(T_i, \theta_j)} - 1 \right\|, \tag{15}$$

where F_{obj} is the objective function. $I_*(T_i, \theta_j)$ is the outgoing radiation or radiation response signal on the right side in the θ_i direction when the left wall temperature is T_i in different cases. The subscript "est" and "exp" represent the calculated radiation response signal and the measured radiation response signal according to the current solution position in the search space, respectively. T_i is the sampling temperature, $T_i \in [300, 1000]$. θ_i is the Sampling angle, $\theta_i \in [0°, 90°)$.

Considering the interference in the actual measurement, random noise was added to the measurement results of the simulation experiment. On the one hand, the real measurement results were simulated. On the other hand, the robustness of the CMA-ES algorithm in the radiation inverse problem of the photothermal parameter reconstruction of the medium was tested. The Gaussian error model used in this paper is as follows:

$$I_{\text{exp}}(T_i, \theta_j) = I_{\text{exact}}(T_i, \theta_j) + \sigma\varsigma, \tag{16}$$

where I_{exact} is the accurate measurement result. I_{exp} is the actual measurement result. ς is the standard normally distributed random number with expectation 0 and variance 1. σ is the standard deviation, the calculation formula of σ is as follows:

$$\text{RMSE} = \sqrt{\frac{1}{N_{\text{var}}} \sum_{i=1}^{N_{\text{var}}} (X_{\text{ext},i} - X_{\text{exact},i})^2}, \tag{17}$$

where X_{ext} and X_{exact} respectively represent the estimated value and the true value of the parameters to be inverted. N_{var} is the dimension of the search space of the optimization algorithm, that is the number of parameters to be inverted.

The distribution of absorption coefficient and refractive index in the dispersion medium still has the property of gradient, which is shown as follows:

$$\kappa_a(x) = \begin{cases} a_1, & 0 \le x \le L/2 \\ b_1, & L/2 < x \le L \end{cases} \quad n(x) = \begin{cases} a_2, & 0 \le x \le L/2 \\ b_2, & L/2 < x \le L, \end{cases} \tag{18}$$

where a_1, b_1, a_2, b_2 represent the coefficient of linear distribution, respectively. L represents the total thickness of

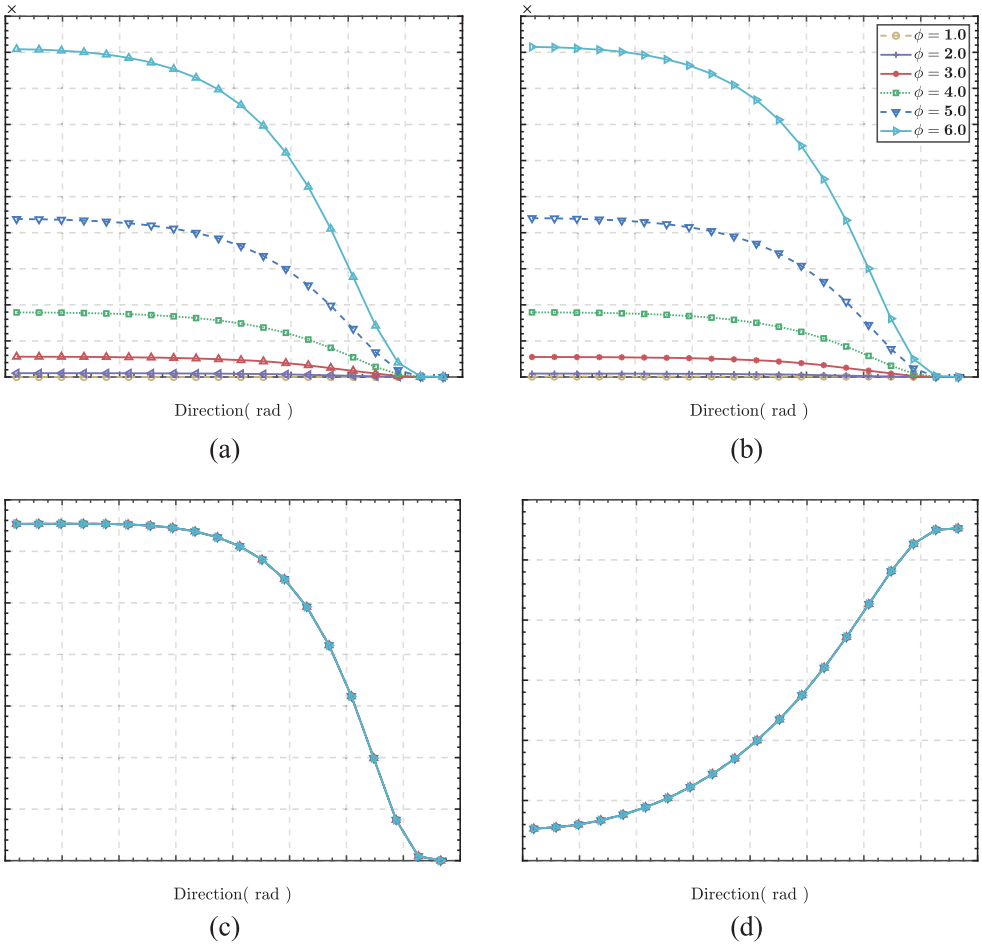

Fig. 7. Sensitivity analysis of parameters to be inverted. (a) a_1, (b) b_1, (c) a_2, (d) b_2.

the dispersion medium. This paper assumes that the thickness of the two sub media is the same. At the same time, they are the assumed parameter of the parameter inversion experiment and the parameter to be inverted of the reconstruction algorithm. x is the normalized spatial position of the thickness of the medium as the characteristic length.

3.3 Sensitivity analysis of absorption coefficient and refractive index of multilayer dispersive media

The outgoing radiation response signals at multiple angles at the right boundary under different wall temperatures are required as known information in the reconstruction algorithm of spectral characteristic parameters of dispersive media based on the CMA-ES algorithm. The ratio of wall temperature to medium temperature is φ:

$$\varphi = \frac{T_{\text{in}}}{T_w}. \tag{19}$$

The output radiation response signal varies with the temperature ratio φ and the exit angle θ. To quantitatively analyze the relationship between the inversion parameters and the outgoing radiation response signal, the concept of sensitivity is introduced in this paper. The sensitivity describes the sensitivity between two sets of variables: when the sensitivity coefficient is small, the measured signal is less affected by the parameters to be inverted. Even without measurement error, it is difficult to reconstruct the inversion parameter distribution accurately according to the current measured signal. When the sensitivity coefficient is large, the measured signal varies greatly with the change of parameters to be inverted. When there is no measurement error, the precise inversion of parameters can be realized simply. However, when there is a small error in the measured signal, there will be a large deviation between the inversion result and the actual result.

When the sensitivity coefficient is large or small, the sensitivity of the inversion parameters can be adjusted by constructing an appropriate objective function to improve the computational efficiency of the reconstruction algorithm and the accuracy of the results. But it does not solve the problem from the root. In this paper, another idea is adopted to select the temperature ratio φ and exit angle θ corresponding to the output radiation response signal through the sensitivity coefficient. To improve the calculation efficiency, the accuracy of the results, and the robustness of the algorithm for the reconstruction of photothermal parameters of dispersive media.

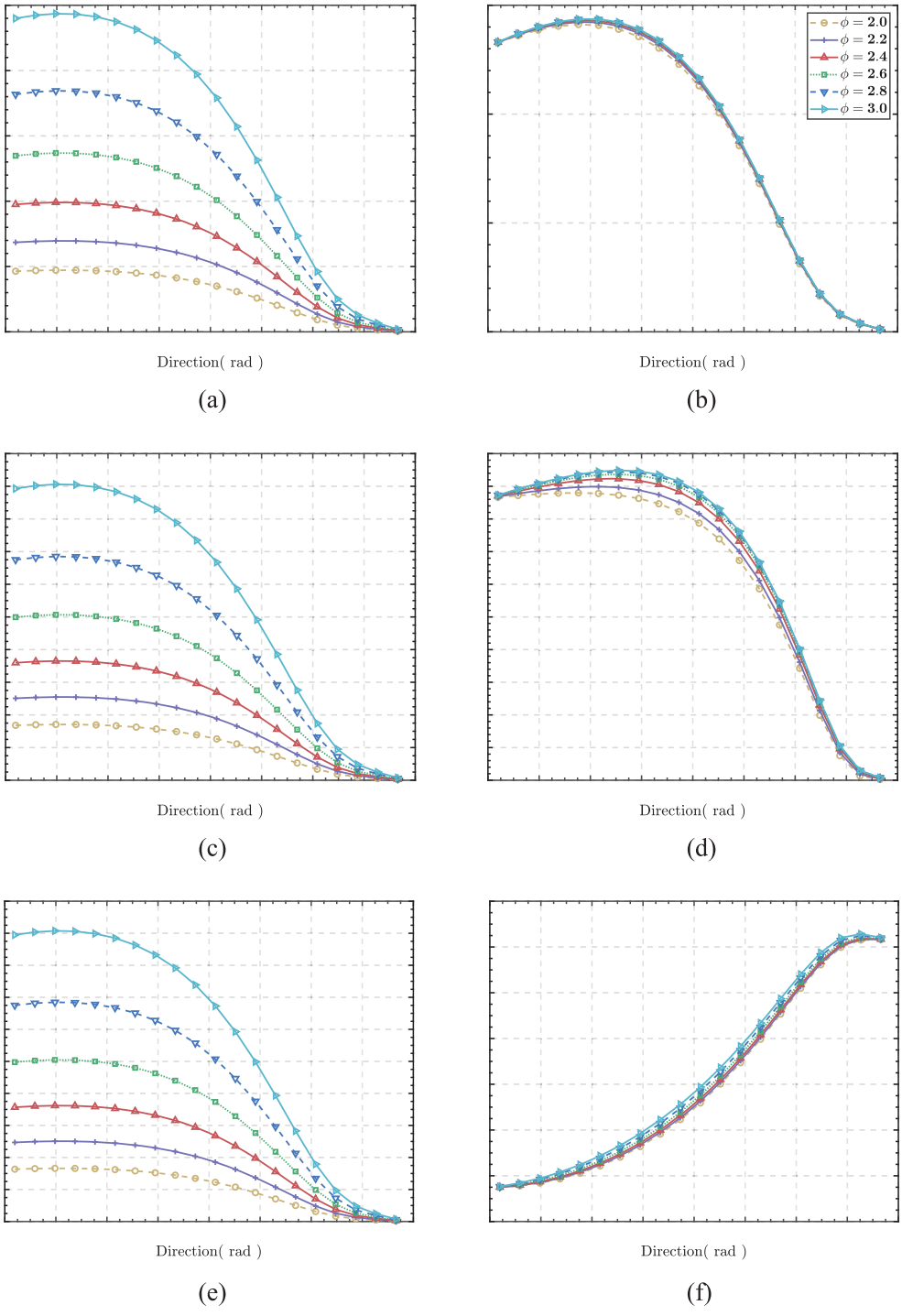

Fig. 8. Sensitivity analysis of parameters to be inverted for three-layer media. (a) a_1, (b) a_2, (c) b_1, (d) b_2, (e) c_1, (f) c_2.

The sensitivity coefficient can be calculated by taking the derivative of one variable to another variable. The sensitivity coefficient adopted in this paper can be calculated according to the following formula:

$$S_{x_i}\left(I^x_{\varphi,\theta}\right) = \left.\frac{\partial I^x_{\varphi,\theta}}{\partial x_i}\right|_{x_i=x_0} = \frac{\left|I^x_{\varphi,\theta}(x_0 + x_0\delta) - I^x_{\varphi,\theta}(x_0 - x_0\delta)\right|}{2x_0\delta}, \tag{20}$$

where S_{x_i} is the sensitivity coefficient of the variable x_i to the measured signal. $I^x_{\varphi,\theta}$ represents the radiation response signal in the φ direction along the angle between the right boundary and the normal direction of the surface when the temperature ratio is θ, x_i is the i parameter to be inversed, and its true value is x_0. δ is a small rate of change, in this paper δ is 0.5%.

In the two-sided medium model, the sensitivity coefficient relative to the radiation response signal is shown in

Table 2. Inversion results of absorption coefficient and refractive index of double-layer media model.

SNR (dB)	Coefficient	Absorption coefficient		Refractive index	
		Calculation result	RMSE	Calculation result	RMSE
100	a	$1.000 \pm 6.32 \times 10^{-19}$	$<10^{-4}$	$1.200 \pm 6.61 \times 10^{-19}$	$<10^{-4}$
	b	$1.500 \pm 6.51 \times 10^{-19}$		$1.800 \pm 6.00 \times 10^{-22}$	
80	a	$1.000 \pm 5.24 \times 10^{-8}$	$<10^{-4}$	$1.200 \pm 8.03 \times 10^{-8}$	$<10^{-4}$
	b	$1.500 \pm 5.26 \times 10^{-8}$		$1.800 \pm 5.40 \times 10^{-12}$	
60	a	$0.999 \pm 5.81 \times 10^{-6}$	6.47×10^{-4}	$1.199 \pm 6.47 \times 10^{-6}$	6.17×10^{-4}
	b	$1.501 \pm 5.82 \times 10^{-6}$		$1.800 \pm 1.53 \times 10^{-9}$	
40	a	$0.991 \pm 3.59 \times 10^{-4}$	8.96×10^{-3}	$1.187 \pm 3.82 \times 10^{-4}$	9.30×10^{-4}
	b	$1.509 \pm 3.80 \times 10^{-4}$		$1.800 \pm 8.39 \times 10^{-8}$	
30	a	$1.010 \pm 1.98 \times 10^{-3}$	1.02×10^{-2}	$1.201 \pm 4.44 \times 10^{-3}$	3.40×10^{-4}
	b	$1.490 \pm 1.95 \times 10^{-3}$		$0.591 \pm 3.02 \times 10^{-8}$	

Figure 7 under the premise of different temperature ratios and different exit radiation angles of the absorption coefficient and refractive index of each sub-medium. Figures 7a and 7b correspond to the absorption coefficients of the two-layer media. The data show that the sensitivity of the absorption coefficient of the two-layer medium is greatly affected by the temperature ratio and the sensitivity coefficient decreases with the increase of the angle θ between the exit direction and the plane normal. The sensitivity of the refractive index of the two-layer medium is less affected by the temperature ratio. With the increase θ, the sensitivity coefficient of the refractive index of the first layer does not change at first and then decreases rapidly. The sensitivity coefficient of the second layer increases with the increase of θ. The trends of the two are not the same.

The essential reason for this difference is that the changes a_2 b_2 have different effects on the gradient refractive index distribution. It is assumed that the distribution of the gradient refractive index is linear, and a_2 b_2 correspond to the starting point and endpoint of the distribution function, respectively. Where a_2 increases, corresponding to the increase of the starting point of the distribution function curve, the slope of the function (the highest coefficient of the function polynomial) decreases, that is the change of a_2 is opposite to that of the function slope, so the changing trend of the sensitivity coefficients of the two is also opposite. The sensitivity coefficient of the linear distribution slope increases with the increase of the included angle θ when the temperature ratio is fixed, which corresponds to the decrease of the sensitivity coefficient a_2 with the increase of θ in Figure 7c. The same analysis is carried out b_2.

The above analysis is extended to the high-dimensional case, and the distribution of the corresponding gradient absorption coefficient and refractive index can be expressed by considering the relatively simple but representative three-layer medium model.

As in the two-dimensional case, the sensitivity coefficient of the absorption coefficient of the three-layer medium has the same trend as the angle. The sensitivity coefficient decreases gradually at the same temperature ratio from left to right. There is a large gap between the first layer and the second layer because the first layer absorbs more radiation energy and plays a leading role. The changing trend of the sensitivity coefficient of the absorption coefficient of the three-layer medium is different. The first two layers decrease with the increase of θ, the third layer increases with the increase of θ. The reason is that the increase of the refractive index of the first two layers will decrease the quadratic coefficient corresponding to the distribution of the quadratic function of the refractive index and the sensitivity of the quadratic coefficient increases with the increase θ. Therefore, the refractive index of the first two layers shows the changing trend as shown in Figures 8b and 8d. By the same token, the variation trend of the sensitivity coefficient of the refractive index of the third layer medium in Figure 8f can also be explained.

According to the calculation results shown in Figure 8, the temperature ratio φ selected in this study is set as 2.3, and the value of the angle is the same as that when the gradient refractive index is distributed in a functional form.

As can be seen in Figure 8, the sensitivity coefficient of the refractive index of the medium increases sequentially from left to right and the sensitivity coefficient of the second layer is about that of the third layer, which leads to the application of the intelligent algorithm to retrieve the gradient refractive index of the medium. The first two layers may not be able to get more accurate results even when there is no measurement error, so the inversion is very difficult. In theory, the directional radiation response signal on the left can be added as the measurement information. Considering that in the direct problem model selected in this chapter, the left side is the opaque wall. Therefore, this paper only uses the directional radiation response signal on the right side as the measurement information in the gradient refractive index inversion experiment of three-layer media and inverts the distribution of three groups of absorption coefficient and refractive index without adding measurement error. Five times of independent inversion in each case. The selection of temperature ratio is the same as that in the inversion of photothermal characteristic parameters of two-layer media in inversion.

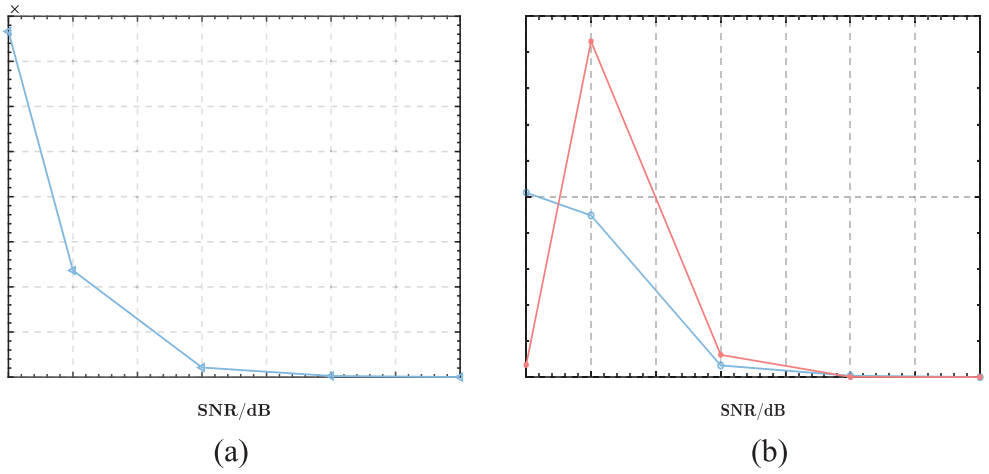

Fig. 9. The fitting function and RMSE change with SNR. (a) Body-fitting function, (b) RMSE.

Table 3. Inversion results of absorption coefficient and refractive index of three-layer media model.

Group	Coefficient	Absorption coefficient		Coefficient	Refractive index	
		Calculation result	RMSE		Calculation result	RMSE
1	$a_1 = 0.5$	$0.500 \pm 1.09 \times 10^{-16}$	1.63×10^{-8}	$a_2 = 1.2$	$1.200 \pm 4.25 \times 10^{-16}$	1.16×10^{-8}
	$b_1 = 1.0$	$1.000 \pm 8.60 \times 10^{-16}$		$b_2 = 1.6$	$1.600 \pm 7.50 \times 10^{-17}$	
	$c_1 = 1.5$	$1.500 \pm 3.22 \times 10^{-16}$		$c_2 = 1.8$	$1.800 \pm 2.68 \times 10^{-22}$	
2	$a_1 = 0.3$	$0.300 \pm 1.01 \times 10^{-17}$	1.57×10^{-9}	$a_2 = 1.2$	$1.200 \pm 5.86 \times 10^{-17}$	4.35×10^{-10}
	$b_1 = 0.4$	$0.400 \pm 3.41 \times 10^{-17}$		$b_2 = 1.6$	$1.600 \pm 6.86 \times 10^{-17}$	
	$c_1 = 0.5$	$0.500 \pm 3.43 \times 10^{-17}$		$c_2 = 1.8$	$1.800 \pm 1.46 \times 10^{-21}$	
3	$a_1 = 0.5$	$0.500 \pm 6.37 \times 10^{-17}$	8.10×10^{-9}	$a_2 = 0.2$	$0.200 \pm 2.26 \times 10^{-12}$	7.67×10^{-9}
	$b_1 = 1.0$	$1.000 \pm 5.17 \times 10^{-16}$		$b_2 = 0.6$	$0.600 \pm 7.47 \times 10^{-17}$	
	$c_1 = 1.5$	$1.500 \pm 1.71 \times 10^{-16}$		$c_2 = 0.8$	$0.800 \pm 1.15 \times 10^{-22}$	

3.4 Joint inversion of absorption coefficient and refractive index for multilayer dispersive media

Firstly, the inversion of absorption coefficient and refractive index of double-layer media under the condition of adding different measurement errors is analyzed. The calculated results are shown in Table 2. The variance of all inversion results is less than 10^{-4}, indicating that a total of 50 inversions included in this inversion experiment have achieved convergence.

The data show that the average value of the inversion results is close to the truth value of the parameters to be inverted and the error is small. It indicates that the reconstruction algorithm of the photothermal characteristics parameters of the dispersion medium constructed in this section for the bilayer medium model can calculate the true value of the inversion under the condition of the existence of errors.

The RMSE statistics of the results can obtain better measurement results even with large measurement errors. However, there are fluctuations in the RMSE data of the refractive index inversion results when the SNR of the added error is equal to 30 dB and 40 dB, which do not increase with the increase of the SNR. Moreover, the comparison of the data shows that the RMSE values of the two cases are very close. This paper believes that the reason for this phenomenon is the randomness of the inversion algorithm, so the results of this calculation are contingent.

The aptamer function and RMSE vary with SNR as shown in Figure 9. The value of aptamer function in Figure 9a increases with the decrease of signal-to-noise ratio, the maximum value is less than 8×10^{-4}. The fluctuation described above can be seen in the red line in Figure 9b. Corresponding to the axis on the right, it can be seen that the maximum value of the axis is only 0.01. The data in the figure further verify the reliability of the inversion algorithm.

The inversion of absorption coefficient and refractive index of three-layer media is analyzed below. The inversion results are shown in Table 3. The data show that good measurement results have been obtained from the three sets of inversion. Comparing the measurement results of the absorption coefficient and the refractive index, it is found that the standard deviation of the three-layer absorption

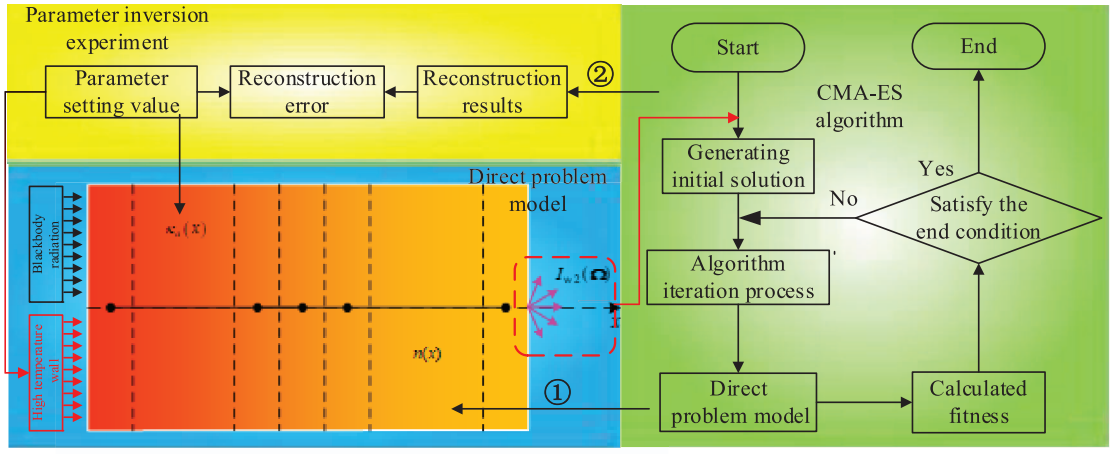

Fig. 10. Experimental flow chart of wall temperature inversion.

Table 4. Experimental calculation results of wall temperature inversion.

SNR (dB)	$T_{w1} = 1000$ K		$T_{w2} = 1500$ K	
	Calculation result	Error	Calculation result	Error
100	$1000.00 \pm 1.77 \times 10^{-17}$	5.43×10^{-12}	$1500.00 \pm 2.84 \times 10^{-17}$	5.34×10^{-11}
80	$1000.00 \pm 6.91 \times 10^{-8}$	5.71×10^{-6}	$1500.00 \pm 1.83 \times 10^{-7}$	6.06×10^{-6}
60	$1000.00 \pm 1.01 \times 10^{-5}$	7.24×10^{-5}	$1500.00 \pm 1.96 \times 10^{-5}$	1.74×10^{-4}
40	$1000.00 \pm 1.35 \times 10^{-3}$	1.01×10^{-4}	$1500.00 \pm 2.07 \times 10^{-3}$	1.84×10^{-3}
30	$1000.00 \pm 2.37 \times 10^{-2}$	3.37×10^{-7}	$1500.00 \pm 2.08 \times 10^{-2}$	1.52×10^{-4}

coefficient reconstruction results is of the same or similar magnitude. But the standard deviation of the refractive index reconstruction results decreases gradually from left to right. In the sensitivity analysis of the three-layer medium model, the sensitivity of the refractive index increases gradually with the order of the medium from left to right. There is a large gap between the sensitivity coefficients of the two adjacent layers. This difference in sensitivity will lead to poor accuracy of the inversion results when there is a large error. Based on sacrificing the calculation time, the accuracy of reconstruction can be improved by increasing the directional radiation response signal under different temperature ratios.

3.5 Inversion analysis of temperature of high-temperature wall obscured by dispersive media

Based on the previous reconstruction algorithm of photothermal characteristic parameter distribution of dispersion medium, this paper constructs the reconstruction algorithm of wall temperature under the condition of dispersion medium shadowing. The direct problem model refers to Figure 5. In this paper, it is assumed that the distribution of photothermal parameters of the medium is in the discrete form shown in equation (18). Taking the directional radiation response signal at the right wall as the measurement data input based on knowing the emissivity of the left wall. The wall temperature is inversed to realize the wall temperature measurement under the shadowing condition.

The following inversion experiments are carried out on the proposed wall temperature inversion algorithm. The flow chart of the experiment is shown in Figure 10. In the figure, ① indicates that the inversion results of photothermal parameters of the dispersion medium are brought back to the direct problem model. ② Indicates that the error calculation is carried out for the inversion results of the wall temperature.

In the inversion experiment, the calculation result corresponding to SNR = 30 dB in Table 2 is used as the calculation result of the first step, the direct problem model is used to invert the wall temperature. The inversion was carried out under two conditions: no measurement error and added measurement error. The algorithm was independently run 10 times in each case. We statistically analyzed the average, standard deviation, and average measurement error of the calculated results.

The calculation results are shown in Table 4. The data show that in the wall temperature inversion method proposed in this section, the calculation error tolerance for the first step is large. Even if the first step of the direct problem is based on the measured signal with a high signal-to-noise ratio, the inversion of temperature in the second step can still obtain better results.

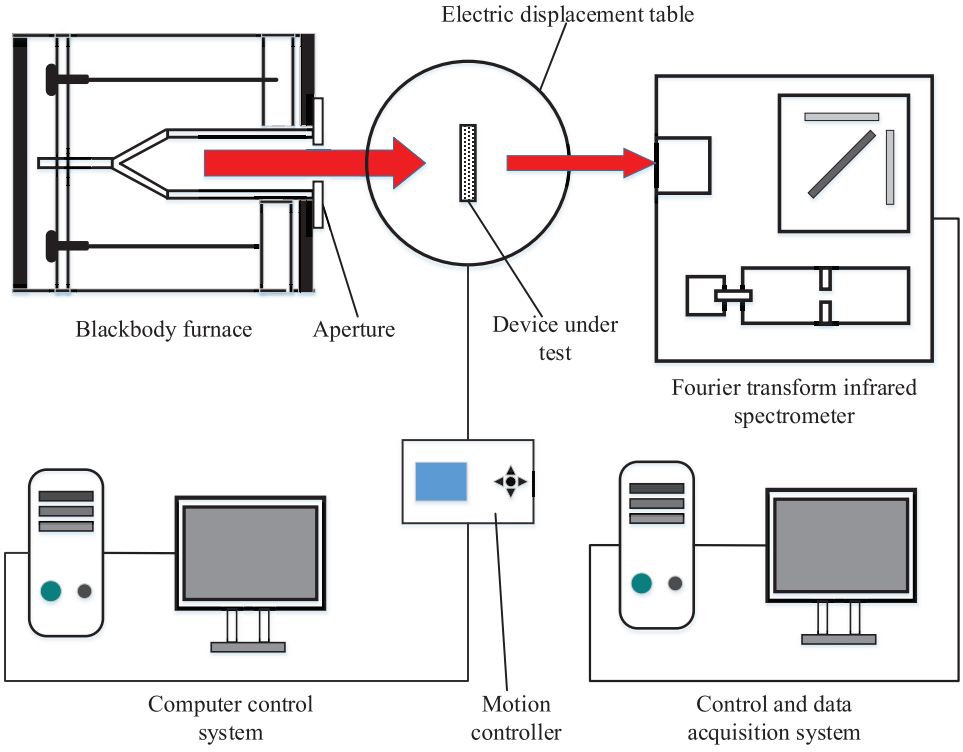

Fig. 11. Measurement system for radiation signal of a translucent body.

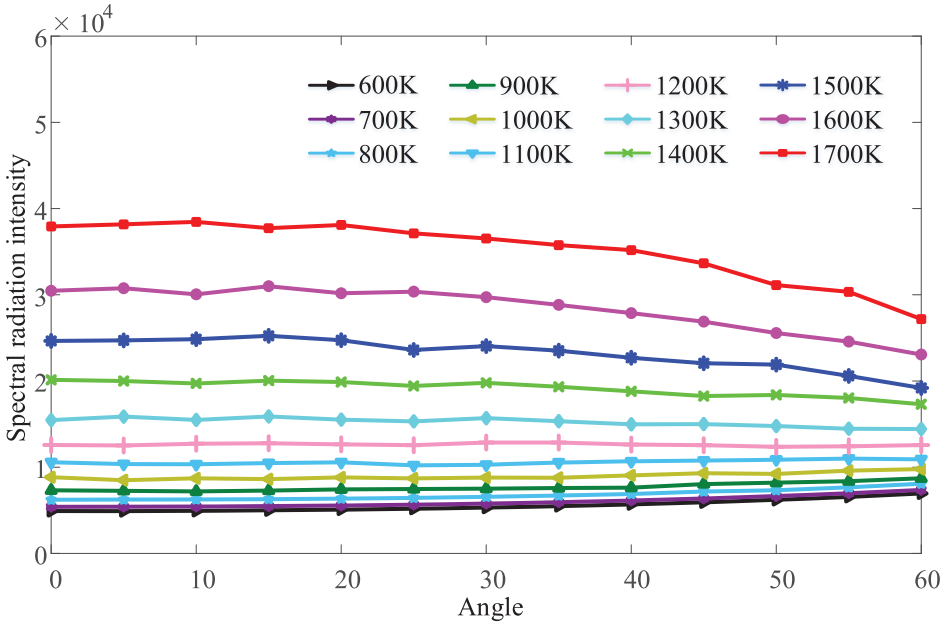

Fig. 12. Spectral signal intensity under different wall temperatures and sample rotation angles.

4 Results and discussion

4.1 Measuring result

The system consists of five parts: black body furnace, Fourier transform infrared spectrometer, electric control rotary table, control, and data acquisition system and test components. Using the experimental platform to measure the radiation signal of the translucent medium. Figure 11 shows the schematic diagram of the measurement system.

In the direct problem model, the radiation signal I is a function of the wall temperature T_w, the refractive index

Table 5. Inversion results of T_w.

Truth value	T_w	1400 K	1500 K	1600 K	1700 K
Inversion value	T_{w0}	1434.62 K	1515.41 K	1599.25 K	1688.74 K
RESM		2.47%	1.03%	0.05%	0.66%

Table 6. Inversion results using different spectral radiation intensities as known information.

Truth value	$\lambda = 5.00$ μm	RESM	$\lambda = 10.53$ μm	RESM	$\lambda = 16.00$ μm	RESM
κ_{a1}	0.227		0.240		0.256	
κ_{a2}	0.039		0.262		0.146	
$T_1 = 1400$ K	1399.49	3.64%	1379.08	1.49%	1388.30	0.84%
$T_2 = 1500$ K	1499.73	0.18%	1474.58	1.69%	1482.74	1.15%
$T_3 = 1600$ K	1600.24	0.02%	1570.69	1.83%	1578.08	1.37%
$T_4 = 1700$ K	1701.01	0.06%	1667.47	1.91%	1683.51	0.97%

n_1 of the first sample, the extinction coefficient κ_{a1} of the first sample, the refractive index n_2 of the second sample, and the extinction coefficient κ_{a2} of the second sample. The size and material of the two plates are the same and the same amount of smoke is injected into the two dishes at the same time during the experiment, so it is considered that the optical properties of the two samples are completely similar.

First of all, the n_1, n_2, κ_{a1} and κ_{a2} of the two-layer samples are inversed, and different angles are measured experimentally (the measuring angle refers to the angle between the normal of the light surface of the sample and the incident light source, the angle of this experiment is from 0° to 60°, every 5° is a measuring point) and different wall temperatures (the wall temperature is the temperature of the blackbody furnace, the temperature range of this experiment is from 600 K to 1700 K, every 100 K is a measuring point). The spectral radiation signal intensity at the wave number 399.1927–4001.5688 cm^{-1}.

Planck integral is introduced to process the measured radiation signals at different wavelengths and the radiation characteristic parameters of the colorimeter in this paper. The formula is as equations (21) and (22). After deducting background noise and Planck integral processing by the double-temperature method, the radiation intensity of different wall temperatures and different sample rotation angles was obtained, as shown in Figure 12:

$$I(T) = \int_{2.5}^{25} I(\lambda, T)\mathrm{d}\lambda, \tag{21}$$

$$n = \int_{2.5}^{25} \frac{n(\lambda)}{25-2.5}\mathrm{d}\lambda \quad \kappa_a = \int_{2.5}^{25} \frac{\kappa_a(\lambda)}{25-2.5}\mathrm{d}\lambda. \tag{22}$$

The initial search range κ_{a1} κ_{a2} is set to 0 to 1 when the algorithm is used for inversion. The refractive index of smoke in the sample is similar to that of air, so the initial search range n_1 and n_2 is set to 1.000 to 1.005. The inversion result is: $n_1 = 1$, $n_2 = 1$, $\kappa_{a1} = 0.192$, $\kappa_{a2} = 0.187$. There is little difference between κ_{a1} and κ_{a2}, n_1 and n_2, which confirms the assumption that the optical properties of the two samples are similar.

Then, n_1, n_2, κ_{a1} and κ_{a2} obtained in the first step are used as known conditions to invert the wall temperature T_w into the direct problem model. In this inversion, the radiation signal measured when the temperature T_w of the blackbody furnace is 1400 K, 1500 K, 1600 K, and 1700 K is inverted by a random algorithm. The initial search temperature range set by the random algorithm is 100–2000 K. The wall temperature T_{w0} obtained by inversion is shown in Table 5.

The results show that the maximum error is less than 1% when the temperature is higher. As the true value of the wall temperature gradually decreases, the inversion accuracy gradually increases. The maximum is less than 3%. It proves the effectiveness and reliability of the wall temperature inversion algorithm based on the intelligent algorithm proposed in this paper under the condition of dispersion medium shielding.

The spectral radiation intensity of the sample at 5 μm, 10.53 μm and 16 μm at different rotation angles and different wall temperatures was measured on the experimental bench to verify the accuracy of the data processed by the Planck integral method. The inversion of k_1 and k_2 was carried out by the algorithm. Then, k_1 and k_2 obtained by inversion are used as known quantities. The spectral radiation intensities measured at different wavelengths at $T_1 = 1400$ K, $T_2 = 1500$ K, $T_3 = 1600$ K and $T_4 = 1700$ K are combined to invert the wall temperature of the blackbody furnace by the algorithm. Table 6 shows the inversion results of experimental data obtained by the Planck integral method and the inversion results without Planck integral.

It can be seen from the above table that there is little difference between the inversion results obtained by the Planck integral method and those without Planck integral, which proves the correctness of using Planck integral to calculate the measurement information as the input of the inversion algorithm.

The tubular furnace is widely used for heating equipment in petrochemical plants. A tube furnace involves a variety of hydrocarbon chemical reactions, as a hydrocarbon energy system. The effective measures to improve the thermal efficiency of the tubular furnace are to use refractory materials with low thermal conductivity and to reduce the temperature of the external wall of the furnace to reduce heat loss. However, the improvement of the thermal efficiency of a tubular furnace is restricted by many factors. Combustion temperature measurement technology provides a direction for improving the thermal efficiency of the tubular furnace.

The calculated results show that the designed temperature reconstruction algorithm can obtain more accurate results when the temperature is less than 1700 K. Take the tubular furnace produced by a certain enterprise as an example. The highest temperature in the furnace can reach 1200 °C, less than 1700 K. Therefore, the algorithm can be used to measure the wall temperature of the tubular furnace and provide direction for its improvement.

4.2 Uncertainty analysis

The errors of κ_{a1} and κ_{a2} inversion in this experiment mainly include the measurement error of the Fourier transforms infrared spectrometer, the temperature error of the blackbody furnace and the angle error of the electric displacement table. The uncertainty of each factor is analyzed below.

1. Uncertainty of Fourier transform infrared spectrometer

The uncertainty of the radiation intensity measured by the spectrometer can be divided into two types: The first type is the measurement error caused by the background noise in the measurement environment and the noise in the measurement process. It has been eliminated by the double-temperature method above. The second type is the measurement error caused by the nonlinear spectral response of the instrument, which is the main source of the measurement error of the Fourier transform infrared spectrometer. The uncertainty of the nonlinear spectral response of the FTIR-6100 spectrometer in this experiment is 0.32%.

2. The uncertainty of blackbody furnace temperature

The uncertainty of the temperature of the blackbody furnace is mainly caused by the fluctuation of the heating circuit under PID control. The temperature of the resistance wire will fluctuate up and down near the target temperature with the increase of time and the amplitude of fluctuation gradually decreases with the increase of time in the process of reaching the target temperature. The high-temperature blackbody furnace used in this experiment is the RT1500 type blackbody furnace produced by LAND Company in the UK. The effective emissivity of the blackbody furnace is 0.99 ± 0.001. The error range of its temperature heating is ± 0.1 °C. The uncertainty is only 4% when the temperature is 25 °C (at room temperature). The uncertainty decreases gradually with the increase of temperature.

3. The uncertainty of the electric displacement table

The angle error of the electric displacement table refers to the difference between the actual rotation angle of the turntable and the set angle. The precision of the Y100SC06 electronic control rotary table is $1 \pm 0.005°$, and the uncertainty is 0.5%.

The above three uncertainties are normally distributed and do not influence each other. Therefore, the overall uncertainty synthesis formula is as follows:

$$U = \sqrt{(U_A)^2 + (U_B)^2 + (U_C)^2}. \tag{23}$$

The formula, U_A represents the uncertainty of the Fourier transform infrared spectrometer, U_B represents the uncertainty of blackbody furnace temperature, and U_C represents the uncertainty of rotation angle of the electronically controlled rotary table. The uncertainty of the system calculated by the above formula is 4.04%. The value is less than 5%, which meets the requirements of extinction coefficient measurement accuracy in the field of most numbers.

5 Conclusion

In this paper, the distribution reconstruction of nonuniform photothermal characteristic parameters of dispersive media based on adaptive covariance matrix evolutionary strategy algorithm is studied. The specific research contents are as follows:

1. Based on the CMA-ES algorithm, the reconstruction program of gradient absorption coefficient and refractive index of functional distribution is established. To obtain a better combination of measurement information, the temperature ratio was defined. The sensitivity of distribution function coefficients was analyzed under different temperature ratios, outgoing radiation, and different surface normal angles. According to the graph line of sensitivity coefficient, the temperature ratio and the included Angle are selected. The reconstruction algorithm is verified and the results show that the algorithm can obtain relatively stable measurement results even with large measurement errors.
2. The more general distribution of photothermal characteristic parameters is considered. The form of the discrete distribution gradient absorption coefficient and refractive index distribution function is unknown during reconstruction. For the two-layer medium model, the sensitivity of absorption coefficient and refractive index is analyzed and the rationality of the image drawn in this paper is explained. The sensitivity graph of absorption coefficient and refractive index of the three-layer medium model is analyzed. The proposed reconstruction algorithm is verified by a two-layer media model and three-layer media model respectively, and the results are good.

3. An inversion algorithm for wall temperature reconstruction under the obscuring condition of dispersive media is proposed. Under the condition of introducing different measurement errors, the effectiveness of the algorithm is verified by experiments. The results show that the performance of the proposed inversion algorithm is good. The proposed algorithm is robust even at higher temperatures. Referring to the internal temperature data of tubular furnaces in the market, the proposed algorithm can be used to provide direction for improving the thermal efficiency of tubular furnaces.

Funding

This research was supported by *National Key R&D Program of China*: 2019YFF0302202.

References

1 Yang S.M., Tao W.Q. (2006) *Heat transfer*, 4th edn, Higher Education Press, Beijing.
2 Wei L.Y. (2020) *Photothermal information simulation and parameter identification in graded-index media*, Harbin Institute of Technology, Harbin. https://doi.org/10.27061/d.cnki.ghgdu.2020.001579.
3 Liu L.H. (2006) Finite volume method for radiation heat transfer in graded index medium, *J. Thermophys. Heat Transf.* **20**, 1, 59–66.
4 Huang Y., Xia X.L., Tan H.P. (2002) Temperature field of radiative equilibrium in a semitransparent slab with a linear refractive index and gray walls, *J. Quant. Spectrosc. Radiat. Transfer* **74**, 2, 249–261.
5 Huang Y., Xia X.L., Tan H.P. (2003) Comparison of two methods for solving radiative heat transfer in a gradient index semitransparent slab, *Numer. Heat Transf. Fundam.* **44**, 1, 83–99.
6 Yong H., Liang X.G., Xia X.L. (2005) Monte Carlo simulation of radiative transfer in scattering, emitting, absorbing slab with gradient index, *J. Quant. Spectrosc. Radiat. Transfer* **92**, 1, 111–120.
7 Ren N., Levoy M., Bredif M., Duval G., Hanrahan P. (2005) *Light field photography with a hand-held plenoptic camera.* Stanford University CTSR.
8 Zhao Z.Y., Nie J.S. (2010) Research on thermal lens effect of grooved laser crystal, *Electro-Optic Technol. Appl.* **05**, 43–45.
9 Xia X.L., Tan H.P., Ren D.P. (2005) Research status of graded-indexthermal radiation and its application prospect in spacecraft technology, *Spacecr. Eng.* **3**, 26–33.
10 Zhang X.P. (2014) Optical analysis of mirage phenomenon, *Friends Phys.* **30**, 10, 18–19.
11 Zhu J.R., Chen YW, Zhang J.Y., Ni H. (2014) The effect of light deflection on interference pattern of flame temperature field with measured by laser, *Lasernal* **2**, 52–53.
12 Wang Z.C. (2013) *A study on radiative heat transfer within 1-D graded-index medium by the Dresor method*, Huazhong University of Science and Technology, Wuhan.
13 Huang Y. (2002) *Study on thermal radiation transfer in graded-index translucent medium*, PhD Thesis in Engineering, Harbin Institute of Technology, Harbin, 12 p.
14 Chandrasekhar S. (1950) *Radiative transfer*, Oxford University Press, New York.
15 Love T.J., Grosh R.J. (1965) Radiative heat transfer in absorbing, emitting, and scattering media, *J. Heat Transf. Am. Soc. Mech. Eng.* **87**, 2, 161–166.
16 Lemonnier D., Le Dez V. (2002) Discrete ordinates solution of radiative transfer across a slab with variable refractive index, *J. Quant. Spectrosc. Radiat. Transf.* **73**, 2, 195–204. Elsevier.
17 Raithby G.D., Chui E.H. (1990) A finite-volume method for predicting a radiant heat transfer in enclosures with participating media, *J. Heat Transf. Am. Soc. Mech. Eng.* **112**, 2, 415–423.
18 Chui E.H., Raithby G.D. (1992) Implicit solution scheme to improve convergence rate in radiative transfer problems, *Numer. Heat Transf. Part B Fundam.* **22**, 3, 251–272. Taylor & Francis.
19 Liu L.H. (2004) Finite element simulation of radiative heat transfer in absorbing and scattering media, *J. Thermophys. Heat Transf.* **18**, 4, 555–557.
20 Zhang L., Zhao J.M., Liu L.H. (2009) Finite element method for modeling radiative transfer in semitransparent graded index cylindrical medium, *J. Quant. Spectrosc. Radiat. Transf.* **110**, 13, 1085–1096. Elsevier.
21 Kim A.D., Ishimaru A. (1999) A Chebyshev spectral method for radiative transfer equations applied to electromagnetic wave propagation and scattering in a discrete random medium, *J. Comput. Phys.* **152**, 1, 264–280. Elsevier.
22 Kim A.D., Moscoso M. (2002) Chebyshev spectral methods for radiative transfer, *SIAM J. Sci. Comput.* **23**, 6, 2074–2094. SIAM.
23 Wei L.Y., Qi H., Niu Z.T., Wen S., Ren Y.T. (2021) Inverse heat transfer analysis to determine the temperature or phase change-dependent refractive index of semitransparent materials, *Inverse Probl. Sci. Eng.* **29**, 4, 586–608.
24 Zhao J.M., Liu L.H. (2007) Solution of radiative heat transfer in graded index media by least square spectral element method, *Int. J. Heat Mass Transf.* **50**, 13, 2634–2642. Elsevier.
25 Zhao J.M., Liu L.H. (2008) Discontinuous spectral element approach for solving transient radiative transfer equation, *J. Thermophys. Heat Transf.* **22**, 1, 20–28.
26 Zhao J.M., Liu L.H. (2008) Spectral element method with adaptive artificial diffusion for solving the radiative transfer equation, *Numer. Heat Transf. Part B Fundam.* **53**, 6, 536–554. Taylor & Francis.
27 Wei L.Y., Sadaf A.I., Wen S. (2018) Simultaneous measurement of space-dependent refractive index and absorption coefficient based on a laser irradiation technique, *Measur. Sci. Technol.* **29**, 10, 104006 (13pp).
28 Hansen N. (2006) The CMA evolution strategy: A comparing review, *Stud Fuzz. Soft Comput.* **192**, 75–102.
29 Hansen N. (2005) *The CMA evolution strategy: A tutorial.* https://lanl.arxiv.org/abs/1604.00772.
30 Hansen N., Ostermeier A. (2001) Completely derandomized self-adaptation in evolution strategies, *Evol. Comput.* **9**, 2, 159–195.
31 Ostermeier A., Gawelczyk A., Hansen N. (1994) A derandomized approach to self-adaptation of evolution strategies, *Evol. Comput.* **2**, 4, 369–380.